Multifrequency Resonant Compensated Wireless Power Transfer SRM Drive System

Jun Cai, *Senior Member, IEEE*, Bin Li, Yangyang Chen, Shoujun Song, *Senior Member, IEEE*, and Xin Zhang, *Senior Member, IEEE*

***Abstract*—In this article, a multifrequency resonant compensated wireless power transfer (WPT) switched reluctance motor (SRM) with zero voltage switching (ZVS) capability is proposed. The system utilizes dual decoupled resonant tanks on the transmitting side and hybrid compensation on the receiving side to achieve multifrequency resonant WPT. In addition, the operating frequencies of the primary inverter are regulated to drive the corresponding SRM phases. The implementation of this method mainly consists of the following steps: First, the number and value of resonant frequencies were optimized to construct multiple power channels, thereby avoiding unexpected energy transfer between the main resonant circuits and overcurrent of the transmitter, and reducing cross-interference between channels. Then, the transmitting coils are overlapped to avoid internal magnetic connections, while the position of the receiving coils is adjusted to realize asymmetric coupling, thereby achieving current equalization in the SRM windings. Moreover, the optimized design of multifrequency resonant compensation networks is developed to reduce the system sensitivity to inductance mismatching and achieve the ZVS of the inverter with the minimized input impedance angle. After that, alternating excitation of single or dual phases can be achieved via a hybrid resonant excitation strategy. Finally, experiments were implemented in a 6/4 SRM-based test-bed, which verified the feasibility of the proposed system.**

***Index Terms*—Cross interference suppression, hybrid resonant excitation strategy, multifrequency resonant compensation (MFRC), switched reluctance motor (SRM), wireless power transfer (WPT), zero voltage switching (ZVS).**

I. Introduction

WIRELESS power transfer (WPT) stems offer distinct advantages such as electrical isolation, convenience, and enhanced safety [1]. Magnetic coupled WPT has undergone extensive research and analysis, encompassing power converters [2], impedance matching networks [3], magnetic couplers [4], efficiency optimized control [5], and so on. Its potential applications include electric vehicle charging [6], wireless lighting [7], intelligent industrial robot driving [8], and pipeline cleaning [9].

Recently, magnetic coupled WPT has been integrated into motor drive [10]. The wireless in-wheel motor has been proposed in [11], in which the wire connections between the wheels and the vehicle body are replaced with a magnetic coupling link to avoid power interruptions caused by vibrations and impacts. However, both the transmitting and receiving sides contain two sets of active converters, resulting in the bulky structure and complex control. In [12], the motor-side dc link voltage control is integrated into the inverter, and secondary parallel compensation is designed to improve system stability, thereby reducing the number of active converters. A WPT switched reluctance motor (SRM) system with an *x*-type converter with minimum number of active switches connecting in the motor side is proposed in [13]. However, the active switches and controllers in the motor side may experience frequent failures in harsh environments.

To avoid regular maintenance of the wireless motor system, special designs have been proposed to eliminate the controller or even active switches in the receiving side. This technology has been applied to stepping motors [14], SRMs [15], [16], [17], [18], [19], induction motors [20], [21], and dc motors [22]. Power transfer methods for such highly reliable wireless motors can mainly be divided into shared-channel transmission and multifrequency multichannel transmission.

Wireless motors with shared power channels usually have multiple transmitters and receivers with the same resonant frequency [14], [15]. Therefore, this system can operate in a resonant state. In addition, the impedance of each transmitting circuit can be individually adjusted to achieve zero voltage switching (ZVS) of the inverter. Furthermore, for selective excitation of multiphase windings, the same-side coils are designed to be mutually decoupled. However, the transmitter of such systems requires at least twice the number of switches as the number of motor phases.

As shown in Fig. 1, the multifrequency multichannel wireless motors adjust the operating frequencies to select power channels and thus excite the target windings. Multiple receivers with different resonant frequencies and a single transmitter are adopted in [16], [17], [18], [19], [20], [21], and [22]. By tuning the inverter's operating frequency to one of the resonant frequencies, the target receiver can be excited. In [16], the transmitter only requires a single-phase full-bridge (FB) inverter. Meanwhile, the LCC compensation network can be designed to balance the power of the SRM windings. However, the transmitter has only

Received 8 October 2024; revised 31 December 2024; accepted 31 January 2025. Date of publication 17 February 2025; date of current version 14 April 2025. This work was supported in part by the National Natural Science Foundation of China under Grant 52477055 and in part by Excellent Research and Innovation Teams in Universities in Anhui Province under Grant 2023AH010021. Recommended for publication by Associate Editor J. Acero. *(Corresponding author: Jun Cai.)*

Jun Cai is with the C-MEIC, CICAEET, and School of Automation, Nanjing University of Information Science and Technology, Nanjing 210044, China, and also with the School of Mechanical and Electrical Engineering, Anhui Jianzhu University, Hefei 230009, China (e-mail: j.cai@nuist.edu.cn).

Bin Li and Yangyang Chen are with the C-MEIC, CICAEET, and School of Automation, Nanjing University of Information Science and Technology, Nanjing 210044, China (e-mail: binli@nuist.edu.cn; chenyangyang@nuist.edu.cn).

Shoujun Song is with the College of Automation, Northwestern Polytechnical University, Xi'an 710072, China (e-mail: sunnyway@nwpu.edu.cn).

Xin Zhang is with the College of Electrical Engineering, Zhejiang University, Hangzhou 310027, China (e-mail: zhangxin_ieee@zju.edu.cn).

Color versions of one or more figures in this article are available at https://doi.org/10.1109/TPEL.2025.3542573.

Digital Object Identifier 10.1109/TPEL.2025.3542573

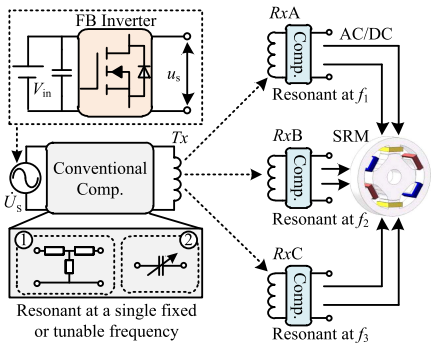

Fig. 1. Conventional multi-frequency multichannel WPT-SRM [16], [17], [18], [19].

one resonant point, resulting in a nonfully resonant state of the multifrequency channels.

To achieve resonance transmission and ZVS in the multichannel WPT-SRM, switched capacitors [17] or tunable compensation networks [18] are employed. Thus, the impedance angles of the transmitter at different operating frequencies can be separately regulated. However, additional switches are required to achieve dynamic adjustment of capacitor values. Meanwhile, the WPT-SRM in [15], [16], [17], and [18] activate the channels one by one and cannot achieve phase-overlapped excitation. To solve the issues and enhance motor output, a decoupled multifrequency multiphase WPT-SRM with trap filters and hybrid single/dual phases driving control strategy is proposed in [19]. However, all the systems in [17], [18], and [19] cannot realize ZVS for multiple power channels. The multichannel ZVS scheme aids in reducing the loss and heat generation of the inverter, significantly enhancing its overall reliability, and effectively mitigating the electromagnetic noise produced during the switching actions of the switching devices.

Simultaneous excitation of multiple channels brings new challenges for WPT-SRM to maintain a resonant state and ZVS. Multiple load-independent resonant points are desired in the system, and the passive multifrequency resonant compensation (MFRC) is considered a viable solution [20], [21], [22]. In [22], MFRC is applied on the receiving side to compensate for the reactive power of coils at multiple frequencies, and resonant tanks with different resonant frequencies are selected by a single pole double throw to achieve ZVS. However, only one channel can be excited at once. When the single resonant tank with MFRC is excited with multiple frequencies simultaneously, hard switching of the inverter occurs [23], [24], [25], [26].

In this article, a multifrequency resonant compensated WPT-SRM system with dual decoupled resonant tanks in the transmitter and ZVS operated inverter is proposed in this article. Specifically, this system can achieve cross interference suppression without the need to introduce additional trap filters networks composed of capacitors and inductors, thereby reducing system costs. When selectively exciting the load, no additional switching devices are required, and the transmitting side can operate in a fully resonant state. The main contributions are as follows.

1) Optimal resonant frequencies are utilized to construct multiple power channels, thereby avoiding unexpected energy transfer between the primary resonant tanks and overcurrent of the transmitter, while reducing cross interference between the channels.
2) The MFRC network is configured in each resonant tank of the transmitter to ensure resonance state of targeted channels. In addition, an optimized design method for the MFRC is proposed to achieve ZVS operation for multiple channels and minimize the input impedance angle, while reducing the sensitivity of current output to compensation elements and enhancing system stability.
3) The position of the receiving coils relative to the transmitting coils is adjusted to realize the asymmetric coupling and achieve the current balance of SRM windings, which can enhance the system efficiency.
4) The hybrid single or dual phase excitation method is achieved, which can help improving the torque output as compared with traditional single phase sequential excitation method.

The rest of this article is organized as follows. The topology and operational principles of the proposed system are given in Section II. Then, the system circuit design and control strategies are presented in Section III. Furthermore, the experimental setup is built to verify the feasibility of the proposed system in Section IV. Finally, Section V concludes this article.

II. Proposed Multifrequency Resonant Compensated WPT-SRM

A. Comparison of the Multifrequency Resonant Compensated WPT-SRM Topologies

The topology of the conventional multifrequency WPT- SRM is shown in Fig. 1, where the transmitting coil and the receiving coils are represented as *Tx* and *Rxm* ($m = \mathrm{A}, \mathrm{B}, \mathrm{C}$), respectively. Although the systems in [17], [18], and [19] achieve ZVS in a time-division way, it cannot simultaneously realize ZVS for multiple power channels.

Hence, the multifrequency resonant compensated WPT- SRM is proposed, which employs two resonant tanks in the transmitter and three receivers with different resonant frequencies, as shown in Fig. 2. Each resonant tank in the transmitting side is equipped with an MFRC network and a transmitting coil, driven by one bridge leg of the FB inverter. The transmitting coils are overlapped to decouple the dual resonant tanks, avoiding direct interference of the tanks.

To alternately excite single and dual phases of the WPT-SRM, the FB inverter is initially controlled as a multifrequency ac excitation source, allowing the transmitter to select single or dual phases by adjusting the operating frequencies. The operation modes are as follows.

1) *Mode I, single-phase excitation mode (SPEM)*: A single resonant tank of the transmitter is excited by the voltage $U_{\mathrm{S1}}^{(1)}$ at frequency f_{o1}, and the other resonant tank is not excited. Then, energy is transmitted to one of the receivers with resonant frequency of f_{o1}.
2) *Mode II, dual-phase excitation mode (DPEM)*: Two resonant tanks of the transmitter are excited by the voltages $U_{\mathrm{S1}}^{(1)}$, $U_{\mathrm{S2}}^{(2)}$ at frequencies f_{o1}, f_{o2} respectively, resulting in two of the receivers being selected as targets and energized.

It is worth noting that each resonant tank of the transmitter operates at a single frequency at once and supplies energy to only one receiver at a time. Therefore, ZVS under SPEM and DPEM can be achieved by ensuring the input impedance of each tank to be inductive.

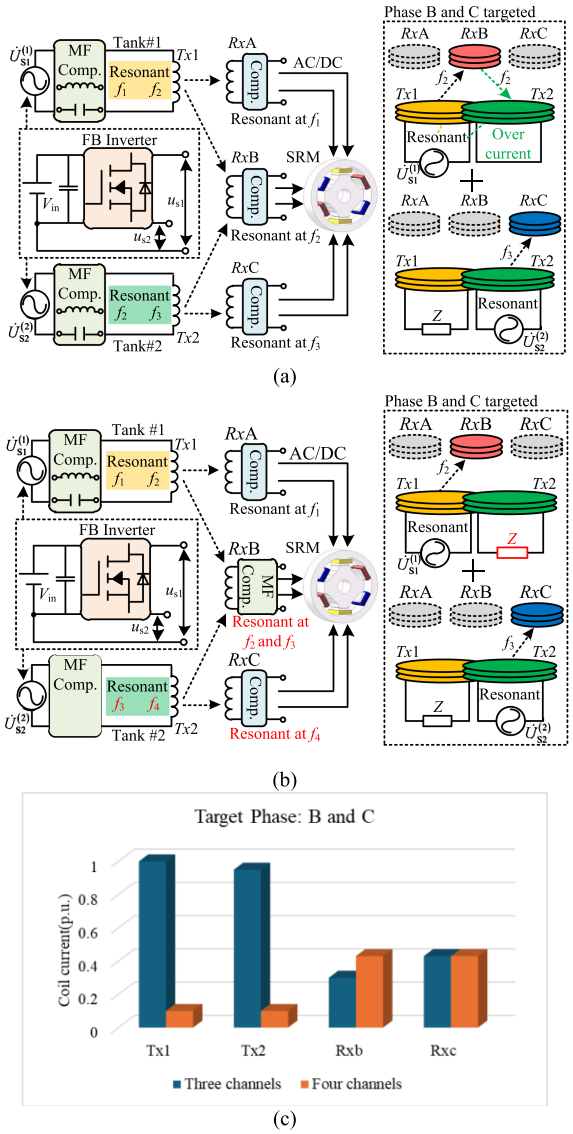

Fig. 2. Comparison of the multifrequency resonant compensated WPT- SRM system topologies. (a) Three channels. (b) Four channels. (c) Normalized coil current.

Two possible implementations of multifrequency resonant compensated WPT-SRM are shown in Fig. 2(a) and (b). Fig. 2(a) shows the WPT-SRM with three channels. In the transmitter, tank #1 resonates at f_1 and f_2, and tank #2 resonates at f_2 and f_3, while the receiver A, B and C resonate at f_1, f_2, and f_3, respectively. Take phase B and C targeted as an example, tank #1 operates at $f_{o1} = f_2$ and tank #2 operates at $f_{o2} = f_3$. Ideally, the power will mainly flow from the transmitter to the receiver B and C. According to the principle of superposition in circuits, the equivalent circuit when each voltage source acts independently on the system can be analyzed separately. When $U_{S2}^{(2)}$ at frequency of f_3 is activated, power can be transferred to phase C because tank #2 and receiver C resonate simultaneously, and tank #1 behaves as a high impedance state. However, when $U_{S1}^{(1)}$ at frequency of f_2 is activated, both tanks of the transmitter resonate with the receiver B. If the resistance inside the compensation element and the coil are ignored, tank #2 will be equivalent to a short circuit. Subsequently, the receiving coil *Rx*B can be considered as a relay coil between the transmitting coils *Tx*1 and *Tx*2. As shown in Fig. 2(c), significant reactive current will occur in the transmitting coils, potentially leading to component burnout. Meanwhile, some power at frequency of f_2 is plundered by tank #2. Hence, the rate load current cannot be ensured.

To solve the above-mentioned problem, a four-channel-based WPT-SRM is proposed as shown in Fig. 2(b). Tank #1 resonates at f_1 and f_2, and tank #2 resonates at f_3 and f_4, which means the resonant frequencies of tank #2 does not overlap tank #1 and the dual tanks are decoupled. The receiver B adopts MFRC with resonant frequencies of f_2 and f_3. Take phase B and C targeted as an example, tank #1 operates at $f_{o1} = f_2$ and tank #2 operates at $f_{o2} = f_4$. When the channel at f_2 is activated, only tank #1 resonates with the receiver B and tank #2 behaves as a high impedance state. Then, the reactive current in transmitting coils can be restricted and the power will mainly flow to receiver B instead of tank #2.

B. Overall Configuration of the Proposed Four-Channel Based Multifrequency Resonant Compensated WPT-SRM

As shown in Fig. 3, the proposed system includes a transmitter and three receivers. The transmitter consists of a dc voltage source V_{in}, a FB inverter and two resonant tanks. Each tank, which is connected to a bridge leg of the inverter, is composed of a dual-frequency resonant network and a transmitting coil. In the resonant tank #*k* ($k = 1, 2$), the dual-frequency resonant network X_{pk} is composed of paralleled inductor L_{pk} and capacitor C_{pk}, as well as series capacitor C_{pFk}. The transmitting coils are decoupled, and the inductance and resistance of *Txk* are L_{Tk} and R_{Tk}, respectively. M_{T12} is the mutual inductance between transmitting coils. M_{Tmk} represents the mutual inductance between the transmitting coil *Txk* and the receiving coil *Rxm*. M_{mg} ($g = $ A, B, C, $m \neq g$) is the mutual inductance between receiving coils. Each receiver consists of a receiving coil, compensation, rectifier, filtering capacitor C_{mf}, and motor winding R_{Lm}. The inductance and resistance of *Rxm* are L_m and R_m. The receiving coils are asymmetrically arranged to balance the current of each phase. The hybrid compensation is utilized in the receiving side. Receiver A and C adopt series capacitors C_A and C_C to compensate for reactive power. Receiver B adopts the MFRC network X_B to simultaneously receive dual-frequency energy and X_B is composed of paralleled inductor L_{B1} and capacitor C_{B1}, as well as series capacitor C_B. u_{Sk} and i_{Sk} are the inverter output voltage and current, respectively; u_m and i_m are the voltage and current of the receiving coil, respectively; u_{Lm} and i_{Lm} are the winding voltage and current, respectively. The resonant frequency in the receiving side is f_j ($j = 1, 2, 3, 4$). Receiver A and C are resonant at f_1 and f_4, respectively, and receiver B is resonant at f_2 and f_3. Then, by regulating the operating frequencies of the inverter to the receivers' resonant frequencies, the power can be transferred to targeted receivers through channels. It should be noted that tank #1 can only excite the phase A or B, while tank #2 can only excite the phase B or C, regardless of the operation modes.

The primary inverter operates differently in different modes, thus enabling the multifrequency ac excitation of the system.

1) In SPEM, two possible states are as follows.
   a) The MOSFETs Q_1 and Q_2 of the bridge leg I are controlled by PWM signals with frequency of f_{o1}. Q_3 and Q_4 of the bridge leg II are cutoff.
   b) Q_1 and Q_2 are cut off, while Q_3 and Q_4 are controlled by PWM signals with frequency of f_{o2}, and $f_{o1} \neq f_{o2}$.

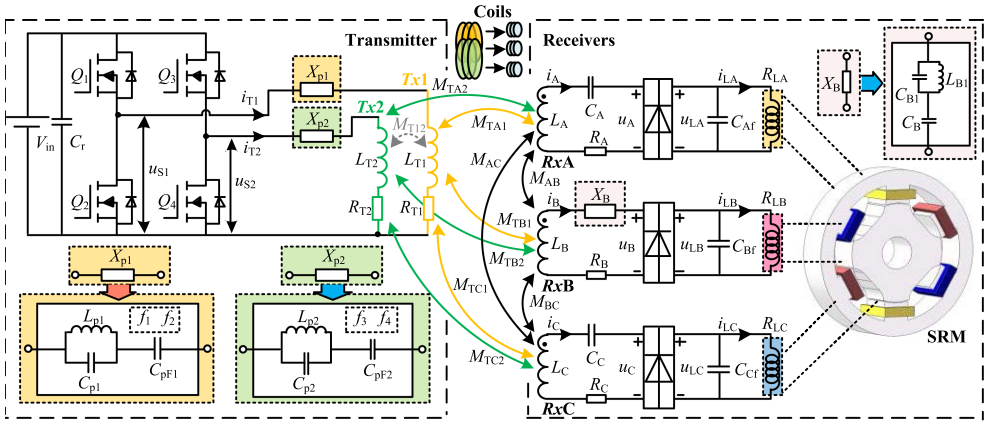

Fig. 3. Configuration of the proposed multifrequency resonant compensated WPT-SRM.

2) In DPEM, Q_1 and Q_2 operate at frequency f_{o1}, while Q_3 and Q_4 operate at frequency of f_{o2}.

C. Modeling of the Proposed System

The equivalent load of the inductive winding in the dc side of the rectifier can be considered as a resistance varied with the motor speed and torque [18]. R_{Leqm} is the load converted to the ac side of the rectifier, where $R_{\mathrm{Leqm}} = (8/\pi^2) \times R_{\mathrm{Lm}}$. The resonant frequencies of parallel LC units in MFRC networks X_{P1}, X_{P2}, and X_{B} are f_{p1}, f_{p2}, and f_{B1}. The angular frequency are $\omega_j = 2\pi f_j$, $\omega_{\mathrm{pk}} = 2\pi f_{\mathrm{pk}}$ and $\omega_{\mathrm{B1}} = 2\pi f_{\mathrm{B1}}$. The impendence X_{P1}, X_{P2}, and X_{B} can be calculated as

$$X_{\mathrm{p1}}(\omega) = \frac{-1}{\omega C_{\mathrm{PF1}}} + \frac{\omega L_{\mathrm{p1}}}{1-\omega^2 L_{\mathrm{p1}} C_{\mathrm{p1}}} = \frac{-1}{\omega C_{\mathrm{PF1}}} + \frac{\omega L_{\mathrm{p1}}}{1-\omega^2 \zeta_1/\omega_2^2} \tag{1}$$

$$X_{\mathrm{p2}}(\omega) = \frac{-1}{\omega C_{\mathrm{PF2}}} + \frac{\omega L_{\mathrm{p2}}}{1-\omega^2 L_{\mathrm{p2}} C_{\mathrm{p2}}} = \frac{-1}{\omega C_{\mathrm{PF2}}} + \frac{\omega L_{\mathrm{p2}}}{1-\omega^2 \zeta_2/\omega_4^2} \tag{2}$$

$$X_{\mathrm{B}}(\omega) = \frac{-1}{\omega C_{\mathrm{B}}} + \frac{\omega L_{\mathrm{B1}}}{1-\omega^2 L_{\mathrm{B1}} C_{\mathrm{B1}}} = \frac{-1}{\omega C_{\mathrm{B}}} + \frac{\omega L_{\mathrm{B1}}}{1-\omega^2 \zeta_{\mathrm{B}}/\omega_3^2} \tag{3}$$

where ζ represents the relationship between the higher resonant angular frequency and the resonant angular frequency of the parallel LC unit in the MFRC network, and $\zeta_1 = (\omega_2/\omega_{\mathrm{p1}})^2$, $\zeta_2 = (\omega_4/\omega_{\mathrm{p2}})^2$ and $\zeta_{\mathrm{B}} = (\omega_3/\omega_{\mathrm{B1}})^2$.

If the internal resistance of the compensation element is ignored, in order to completely compensate the reactive power of the coils at different operating frequencies, the compensation networks should satisfy (4) and (5) to make the reactive impedance to be zero

$$\begin{cases} \omega L_{\mathrm{T1}} + X_{\mathrm{p1}}(\omega) = 0 \quad (\omega = \omega_1 \text{ or } \omega_2) \\ \omega L_{\mathrm{T2}} + X_{\mathrm{p2}}(\omega) = 0 \quad (\omega = \omega_3 \text{ or } \omega_4) \end{cases} \tag{4}$$

$$\begin{cases} \omega_1^2 L_{\mathrm{A}} C_{\mathrm{A}} - 1 = 0 \\ \omega L_{\mathrm{B}} + X_{\mathrm{B}}(\omega) = 0 \quad (\omega = \omega_2 \text{ or } \omega_3) \\ \omega_4^2 L_{\mathrm{C}} C_{\mathrm{C}} - 1 = 0 \end{cases} \tag{5}$$

According to the Kirchhoff's voltage law, the circuit model when tank #1 is activated can be expressed as (6) shown at the bottom of the next page, and the model when tank #2 is excited can be given by (7) shown at the bottom of the next page. In (6) and (7), the superscript i indicates the operating frequency and $\omega_{\mathrm{oi}} = 2\pi f_{\mathrm{oi}}$ ($i = 1, 2$). The value of f_{oi} is one of the resonant frequencies. The impedance of the tank #k can be expressed as

$$Z_{\mathrm{Tk}}^{(i)} = X_{\mathrm{pk}}(\omega_{\mathrm{oi}}) + R_{\mathrm{Tk}}. \tag{8}$$

The impedance of the receivers can be given by

$$Z_{\mathrm{A}}^{(i)} = j\omega_{\mathrm{oi}} L_{\mathrm{A}} + \frac{1}{j\omega_{\mathrm{oi}} C_{\mathrm{A}}} + R_{\mathrm{A}} + R_{\mathrm{Leqm}} \tag{9}$$

$$Z_{\mathrm{B}}^{(i)} = X_{\mathrm{B}}(\omega_{\mathrm{oi}}) + R_{\mathrm{B}} + R_{\mathrm{Leqm}} \tag{10}$$

$$\begin{bmatrix} \dot{U}_{\mathrm{S1}}^{(i)} \\ 0 \\ 0 \\ 0 \\ 0 \end{bmatrix} = \begin{bmatrix} j\omega_{\mathrm{oi}} Z_{\mathrm{T1}}^{(i)} & 0 & -j\omega_{\mathrm{oi}} M_{\mathrm{TA1}} & -j\omega_{\mathrm{oi}} M_{\mathrm{TB1}} & -j\omega_{\mathrm{oi}} M_{\mathrm{TC1}} \\ 0 & Z_{\mathrm{T2}}^{(i)} & -j\omega_{\mathrm{oi}} M_{\mathrm{TA2}} & -j\omega_{\mathrm{oi}} M_{\mathrm{TB2}} & -j\omega_{\mathrm{oi}} M_{\mathrm{TC2}} \\ -j\omega_{\mathrm{oi}} M_{\mathrm{TA1}} & -j\omega_{\mathrm{oi}} M_{\mathrm{TA2}} & Z_{\mathrm{A}}^{(i)} & j\omega_{\mathrm{oi}} M_{\mathrm{AB}} & j\omega_{\mathrm{oi}} M_{\mathrm{AC}} \\ -j\omega_{\mathrm{oi}} M_{\mathrm{TB1}} & -j\omega_{\mathrm{oi}} M_{\mathrm{TB2}} & j\omega_{\mathrm{oi}} M_{\mathrm{AB}} & Z_{\mathrm{B}}^{(i)} & j\omega_{\mathrm{oi}} M_{\mathrm{BC}} \\ -j\omega_{\mathrm{oi}} M_{\mathrm{TC1}} & -j\omega_{\mathrm{oi}} M_{\mathrm{TC2}} & j\omega_{\mathrm{oi}} M_{\mathrm{AC}} & j\omega_{\mathrm{oi}} M_{\mathrm{BC}} & Z_{\mathrm{C}}^{(i)} \end{bmatrix} \begin{bmatrix} \dot{I}_{\mathrm{T1}}^{(i)} \\ \dot{I}_{\mathrm{T2}}^{(i)} \\ \dot{I}_{\mathrm{A}}^{(i)} \\ \dot{I}_{\mathrm{B}}^{(i)} \\ \dot{I}_{\mathrm{C}}^{(i)} \end{bmatrix} \tag{6}$$

$$\begin{bmatrix} 0 \\ \dot{U}_{\mathrm{S2}}^{(i)} \\ 0 \\ 0 \\ 0 \end{bmatrix} = \begin{bmatrix} j\omega_{\mathrm{oi}} Z_{\mathrm{T1}}^{(i)} & 0 & -j\omega_{\mathrm{oi}} M_{\mathrm{TA1}} & -j\omega_{\mathrm{oi}} M_{\mathrm{TB1}} & -j\omega_{\mathrm{oi}} M_{\mathrm{TC1}} \\ 0 & Z_{\mathrm{T2}}^{(i)} & -j\omega_{\mathrm{oi}} M_{\mathrm{TA2}} & -j\omega_{\mathrm{oi}} M_{\mathrm{TB2}} & -j\omega_{\mathrm{oi}} M_{\mathrm{TC2}} \\ -j\omega_{\mathrm{oi}} M_{\mathrm{TA1}} & -j\omega_{\mathrm{oi}} M_{\mathrm{TA2}} & Z_{\mathrm{A}}^{(i)} & j\omega_{\mathrm{oi}} M_{\mathrm{AB}} & j\omega_{\mathrm{oi}} M_{\mathrm{AC}} \\ -j\omega_{\mathrm{oi}} M_{\mathrm{TB1}} & -j\omega_{\mathrm{oi}} M_{\mathrm{TB2}} & j\omega_{\mathrm{oi}} M_{\mathrm{AB}} & Z_{\mathrm{B}}^{(i)} & j\omega_{\mathrm{oi}} M_{\mathrm{BC}} \\ -j\omega_{\mathrm{oi}} M_{\mathrm{TC1}} & -j\omega_{\mathrm{oi}} M_{\mathrm{TC2}} & j\omega_{\mathrm{oi}} M_{\mathrm{AC}} & j\omega_{\mathrm{oi}} M_{\mathrm{BC}} & Z_{\mathrm{C}}^{(i)} \end{bmatrix} \begin{bmatrix} \dot{I}_{\mathrm{T1}}^{(i)} \\ \dot{I}_{\mathrm{T2}}^{(i)} \\ \dot{I}_{\mathrm{A}}^{(i)} \\ \dot{I}_{\mathrm{B}}^{(i)} \\ \dot{I}_{\mathrm{C}}^{(i)} \end{bmatrix}. \tag{7}$$

$$Z_{\mathrm{C}}^{(i)} = j\omega_{\mathrm{oi}}L_{\mathrm{C}} + \frac{1}{j\omega_{\mathrm{oi}}C_{\mathrm{C}}} + R_{\mathrm{C}} + R_{\mathrm{E}}. \tag{11}$$

The rms value of current i_{Tk} and i_{Lm} can be expressed as

$$I_{\mathrm{Tk}} = \sqrt{\left|\dot{I}_{\mathrm{Tk}}^{(1)}\right|^2 + \left|\dot{I}_{\mathrm{Tk}}^{(2)}\right|^2} \tag{12}$$

$$I_{\mathrm{Lm}} = \frac{2\sqrt{2}}{\pi}\sqrt{\left|\dot{I}_{\mathrm{m}}^{(1)}\right|^2 + \left|\dot{I}_{\mathrm{m}}^{(2)}\right|^2}. \tag{13}$$

The angle of the input impedance of the system is

$$\varphi^{(i)} = \begin{cases} \angle\frac{U_{\mathrm{S1}}^{(i)}}{I_{\mathrm{T1}}^{(i)}} & (i=1) \\ \angle\frac{U_{\mathrm{S2}}^{(i)}}{I_{\mathrm{T2}}^{(i)}} & (i=2) \end{cases}. \tag{14}$$

If the cross interference between channels is suppressed, the transmitting coil current $I_{\mathrm{Tk\_ind}}$ in tank #k and the current supplied by tank #k to the load of receiver m, namely $I_{\mathrm{Lmk\_ind}}$, can be given by

$$I_{\mathrm{Tk\_ind}} = \frac{\sqrt{2}}{\pi}\frac{R_{\mathrm{Leqm}}V_{\mathrm{in}}}{R_{\mathrm{Tk}}(R_{\mathrm{m}}+R_{\mathrm{Leqm}}) + (\omega_{\mathrm{oi}}M_{\mathrm{Tmk}})^2} \tag{15}$$

$$I_{\mathrm{Lmk\_ind}} = \frac{4}{\pi^2}\frac{\omega_{\mathrm{oi}}M_{\mathrm{Tmk}}V_{\mathrm{in}}}{R_{\mathrm{Tk}}(R_{\mathrm{m}}+R_{\mathrm{Leqm}}) + (\omega_{\mathrm{oi}}M_{\mathrm{Tmk}})^2}. \tag{16}$$

III. System Design and Control

A. Parameter Design for Balanced Winding Current

To reduce the torque ripple of SRM, the balanced winding current of targeted phases is necessary. Conventional multifrequency WPT-SRMs typically balance the mutual inductance between the transmitting coil and multiple receiving coils, and then adjust compensation parameters to achieve balanced winding current. However, the load current is related to ω_{oi} according to (16), and uniform mutual inductance M_{Tmk} can lead to imbalanced load current of different channels in the proposed system. Therefore, it is required to match M_{Tmk} based on different operating frequencies ω_{oi}, which means the mutual inductance between the transmitting coil and different receiving coils in this system is inconsistent. In the actual design process, by substituting the rated load current I_{ref} into the mathematical model and calculating the expected value of the product of ω_{oi} and M_{Tmk}, balanced outputs for each channel can be achieved.

If cross-interference is considered completely suppressed, and the internal resistance of compensation inductance and capacitance is ignored, the load current is related to V_{in}, ω_{oi}, M_{Tmk}, coil resistance and load. In consideration of the resistance of the transmitting coil, the load current may vary with the load resistance. Assuming $V_{\mathrm{in}} = 96$ V and the rated current requirement $I_{\mathrm{ref}} = 8$ A. In addition, the coil resistance R_{Tk} and R_m can be obtained by measuring the prewound coil, and the system parameters measured in 280 kHz are shown in Table I. Considering magnetic saturation, the range of R_{Lm} changes from 1.3 to 1.8 Ω when the speed of SRM is 0–4000 r/min. Therefore, with the known V_{in}, R_{Tk}, R_m, and R_{Lm}, substituting $I_{\mathrm{Lmk\_ind}} = I_{\mathrm{ref}}$ into (16) and $\omega_{\mathrm{oi}}M_{\mathrm{Tmk}}$ can be solved in (17), providing a basis for the selection of ω_{oi} and M_{Tmk}. It is worth noting that the coil resistance R_{Tk} and R_m vary with the operating frequency ω_{oi}

TABLE I
System Parameters

Items	Value
Inductance of transmitting coil ($L_{\mathrm{T1}}/L_{\mathrm{T1}}$)	383.5/386 μH
Inductance of receiving coils ($L_{\mathrm{A}}/L_{\mathrm{B}}/L_{\mathrm{C}}$)	102.7/44.5/97.9 μH
Mutual inductance between the transmitting coils (M_{T12})	0 μH
Mutual inductance between *Tx*1 and *Rxm* ($M_{\mathrm{TA1}}/M_{\mathrm{TB1}}/M_{\mathrm{TC1}}$)	9.18/3.51/0.62 μH
Mutual inductance between *Tx*1 and *Rxm* ($M_{\mathrm{TA2}}/M_{\mathrm{TB2}}/M_{\mathrm{TC2}}$)	1.5/2.42/5.69 μH
Mutual inductance between the receiving coils ($M_{\mathrm{AB}}/M_{\mathrm{BC}}/M_{\mathrm{AC}}$)	0.67/0.33/0.32 μH
Parallel inductor of MFRC ($L_{\mathrm{p1}}/L_{\mathrm{p2}}/L_{\mathrm{B1}}$)	229.5/203.3/5.1 μH
Parallel capacitor of MFRC ($C_{\mathrm{p1}}/C_{\mathrm{p2}}/C_{\mathrm{B1}}$)	5.24/2.95/88.81 nF
Series capacitor of MFRC ($C_{\mathrm{pF1}}/C_{\mathrm{pF2}}/C_{\mathrm{B}}$)	5.95/2.17/10.16 nF
Series capacitors of receiver A and C ($C_{\mathrm{A}}/C_{\mathrm{C}}$)	39.20/15.39 nF
Resistance of transmitting coil ($R_{\mathrm{T1}}/R_{\mathrm{T2}}$)	1.83/1.71 Ω
Resistance of receiving coil ($R_{\mathrm{A}}/R_{\mathrm{B}}/R_{\mathrm{C}}$)	0.55/0.29/0.53 Ω
Maximum motor winding inductance (L_{max})	5.4 mH
Minimum motor winding inductance (L_{min})	1.3 mH
Motor winding resistance	1.3 Ω
Resonant frequencies of the receivers (f_{i})	80/130/200/280 kHz

$$\omega_{\mathrm{oi}}M_{\mathrm{Tmk}} = \frac{4V_{\mathrm{in}}}{\pi^2 I_{\mathrm{ref}}} + \sqrt{\frac{4}{\pi^2}\left(\frac{V_{\mathrm{in}}}{\pi I_{\mathrm{ref}}}\right)^2 - R_{\mathrm{Tk}}\left(R_m + \frac{8}{\pi^2}R_{\mathrm{Lm}}\right)}. \tag{17}$$

To maintain the winding current balance over the equivalent resistance variation range, $\omega_{\mathrm{oi}}M_{\mathrm{Tmk}}$ can be determined by the following steps.

1) Substitute the center of the equivalent load resistance variation range ($R_{\mathrm{Lm}} = 1.5\ \Omega$) into (17) to calculate $\omega_{\mathrm{oi}}M_{\mathrm{Tmk}}$.
2) Substitute the calculated $\omega_{\mathrm{oi}}M_{\mathrm{Tmk}}$ from step one into (16) and verify current balance within the range of R_{Lm}. If $|I_{\mathrm{Lmk\_ind}}\text{-}I_{\mathrm{ref}}| \le 5\% \times I_{\mathrm{ref}}$ satisfies within the load variation range, use the calculated $\omega_{\mathrm{oi}}M_{\mathrm{Tmk}}$ from step one as the expected value. Otherwise, redesign the coil to reduce coil resistance.

As aforementioned, tank #1 can only activate the phase A or B, while tank #2 can only activate the phase B or C. To prevent tank #1 from energizing phase C, and avoid tank #2 powering phase A, M_{TA2} and M_{TC1} are adjusted to about 0 μH. Hence, only the expected $\omega_1 M_{\mathrm{TA1}}$, $\omega_2 M_{\mathrm{TB1}}$, $\omega_3 M_{\mathrm{TB2}}$, and $\omega_4 M_{\mathrm{TAC2}}$ need to be calculated.

B. Frequency Selection

The resonant frequency design includes two criterions such as cross cross-interference suppression and compensation for ZVS. This section primarily analyzes the former criterion, while the latter one will be discussed in Section III-D. To evaluate the interference of nontarget frequencies on the output of the receiver, and the mutual interference between the dual tanks of the transmitter, two evaluation factors γ_{Rxmk} and γ_{Txk} are defined in (18) and (19).

When the receiver m is excited with tank #k and (18) is satisfied, the interference of nontarget frequencies on the output

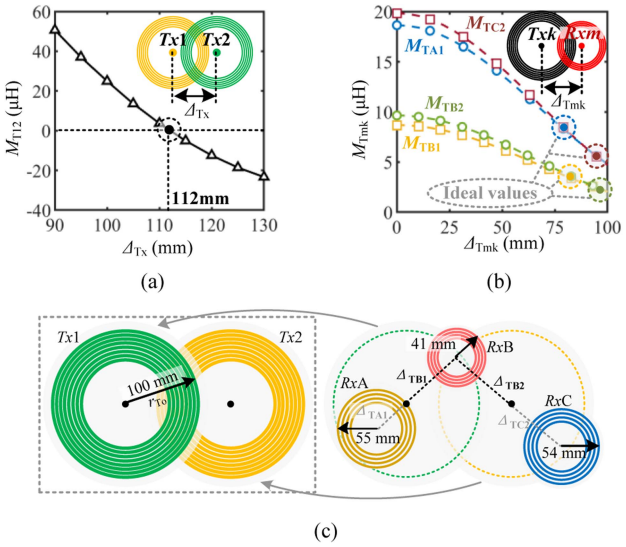

Fig. 4. Coil arrangement and mutual inductance analysis. (a) Relationship between M_{T12} and Δ_{Tx}. (b) Relationship between M_{TA1}, M_{TB1}, M_{TB2}, M_{TAC2} and Δ_{Tmk}. (c) Coil arrangement.

of the receiver can be suppressed

$$\gamma_{\mathrm{Rxmk}} = \frac{|I_{\mathrm{Lm}} - I_{\mathrm{Lmk\_ind}}|}{I_{\mathrm{Lmk\_ind}}} < 5\%. \tag{18}$$

In addition, there may also be mutual interference between the dual tanks of the transmitter. Due to the decoupling of the transmitting coils, this type of interference is usually not directly transmitted between the tanks but is relayed by the receiving coils. If (19) is satisfied, it is considered that the indirect interference of the tanks in the transmitting side can be suppressed

$$\gamma_{\mathrm{Txk}} = \frac{|I_{\mathrm{Tk}} - I_{\mathrm{Tk\_ind}}|}{I_{\mathrm{Tk\_ind}}} < 5\%. \tag{19}$$

To further suppress cross interference, the resonant frequency is chosen to be away from other resonant frequencies and their harmonic frequencies. Since the system operates in open loop with a duty cycle of 0.5, only the interference from odd harmonics of nontarget resonant frequencies needs to be considered. Therefore, f_j should not be close to nf_{w} ($w = 1, 2, 3, 4$, and $w \neq j$; $n = 1, 3, 5\ldots$). The overall design process described in Section III-E of this article can determine the resonant frequencies that meet the requirements of (18) and (19). The selection of f_j can be: $f_1 = 80$ kHz, $f_2 = 200$ kHz, $f_3 = 280$ kHz, $f_4 = 130$ kHz.

C. Coil Arrangement

1) Decoupling of the Transmitting Coils: To avoid direct interference between tanks of the transmitter, an overlapping approach is employed to reduce the mutual inductance M_{T12} to approximately 0 μH. The relationship between the center distance (Δ_{Tx}) of the transmitting coils and M_{T12} can be calculated with finite element analysis, as depicted in Fig. 4(a). It can be seen that decoupling between the dual transmitting coils can be achieved when $\Delta_{\mathrm{Tx}} = 112$ mm.

2) Arrangement of the Receiving Coils: The mutual inductance M_{TA1}, M_{TB1}, M_{TB2}, and M_{TAC2} can be calculated based on the resonant frequency (ω_j) and the expected products of $\omega_1 M_{\mathrm{TA1}}$, $\omega_2 M_{\mathrm{TB1}}$, $\omega_3 M_{\mathrm{TB2}}$, and $\omega_4 M_{\mathrm{TAC2}}$. By fixing the air gap width (h) between the transmitting and receiving coils at 80 mm, the ideal mutual inductance can be achieved by adjusting the horizontal misalignment (Δ_{Tmk}) between the *Txk* and the *Rxm*. The detailed analytical mutual inductance calculation method is as follows.

The mutual inductance between single layer planar circular coil #1and coil #2 is M_{s}, which can be expressed as

$$M_{\mathrm{s}}(h, \Delta) = \sum_{i_1=0}^{N_1-1} \sum_{i_2=0}^{N_2-1} \frac{\mu_0}{4\pi} \iint \frac{\boldsymbol{dl_{i1}} \boldsymbol{dl_{i2}}}{r_{\mathrm{ii}}} \tag{20}$$

where Δ is the horizontal misalignment; N_1 and N_2 are the turns of coils; μ_0 is the vacuum permeability; $\boldsymbol{dl_{i1}}$ and $\boldsymbol{dl_{i2}}$ are the coil length vectors; r_{ii} is the distance between the vectors. $\boldsymbol{dl_{i1}}$, $\boldsymbol{dl_{i2}}$ and r_{ii} can be calculated as

$$\begin{cases} \boldsymbol{dl_{i1}} = r_{\mathrm{i1}}(-\sin\xi \mathbf{x} + \cos\xi \mathbf{y}) d\xi \\ \boldsymbol{dl_{i2}} = r_{\mathrm{i2}}(-\sin\varsigma \mathbf{x} + \cos\varsigma \mathbf{y}) d\varsigma \\ r_{\mathrm{ii}} = [(r_{\mathrm{i1}}\cos\xi - r_{\mathrm{i2}}\cos\varsigma - \Delta)^2 \\ \qquad + (r_{\mathrm{i1}}\cos\xi - r_{\mathrm{i2}}\sin\varsigma)^2 + h^2]^{1/2} \end{cases} \tag{21}$$

where r_{i1} and r_{i2} are the radius of ith turn of the coil #1 and coil #2, respectively; ξ and ς are angle of the vector $\boldsymbol{dl_{i1}}$ and $\boldsymbol{dl_{i2}}$, respectively; $\mathbf{x}$ and $\mathbf{y}$ are the unit vectors. Since the layer of *Txk* is two and the layer of *Rxm* is three, M_{Tmk} can be calculated as

$$\begin{aligned} M_{\mathrm{Tmk}}(h, \Delta_{\mathrm{Tmk}}) &= M_s(h, \Delta_{\mathrm{Tmk}}) + 2M_s(h+p, \Delta_{\mathrm{Tmk}}) \\ &+ 2M_s(h+2p, \Delta_{\mathrm{Tmk}}) + M_s(h+3p, \Delta_{\mathrm{Tmk}}). \end{aligned} \tag{22}$$

where p is the pitch of adjacent layers in a multilayer coil.

The relationship between Δ_{Tmk} and $M_{\mathrm{TA1}}, M_{\mathrm{TB1}}, M_{\mathrm{TB2}}$, and M_{TAC2} can be calculated by (22) and is shown in Fig. 4(b), with the range of Δ_{Tmk} from 0 mm to r_{To}, which is the outer radius of *Txk*. Then, the expected Δ_{TA1}, Δ_{TB1}, Δ_{TB2} and Δ_{TC2} can be located in the curves, and the position of receiving coils can be achieved. As shown in Fig. 4(c), *Rx*A is designed on the lower left side of *Tx*1 to avoid coupling with *Tx*2. Similarly, *Rx*C is designed on the lower right side of *Tx*2, while *Rx*B is designed at the overlap between *Tx*1 and *Tx*2, which can receive the power of Tx1 and *Tx*2 simultaneously.

D. Compensation Design

1) Design for Resonant State and Reduced Sensitivity: Both the transmitter and receiver B employ MFRC to fully compensate for reactive power at both operating frequencies simultaneously. Meanwhile, receiver A and C can be compensated using series capacitors to be resonant at a single frequency. After determining the coils and resonant frequencies, the inductors and capacitors in the MFRC networks $X_{\mathrm{p1}}, X_{\mathrm{p2}}$, and X_{B}, as well as the capacitors C_{A} and C_{C}, can be determined by resonant conditions (4) and (5). The design of network X_{p1} in the tank #1 is taken as an example to expound the calculation method of the parameters in MFRC network. Based on (1) and (4), there is

$$\begin{bmatrix} \frac{1}{C_{\mathrm{pF1}}} \\ L_{\mathrm{p1}} \end{bmatrix} = \begin{bmatrix} \frac{1}{\omega_1} & \frac{\omega_1}{1-\omega_1^2\zeta_1/\omega_2^2} \\ \frac{1}{\omega_2} & \frac{\omega_2}{1-\zeta_1} \end{bmatrix}^{-1} \begin{bmatrix} \omega_1 L_{\mathrm{T1}} \\ \omega_2 L_{\mathrm{T1}} \end{bmatrix}. \tag{23}$$

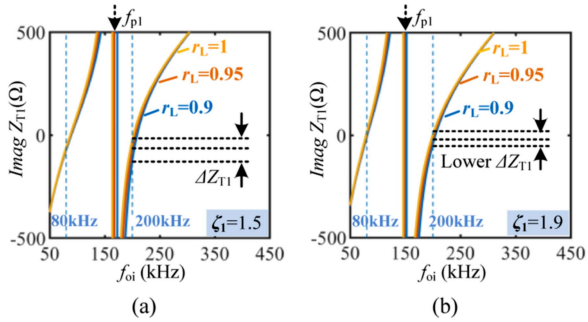

Fig. 5. Relationship between characteristics of imaginary part of Z_{T1} (Imag Z_{T1}) and inductance matching degree r_L in frequency domain. (a) $\zeta_1 = 1.5$. (b) $\zeta_1 = 1.9$.

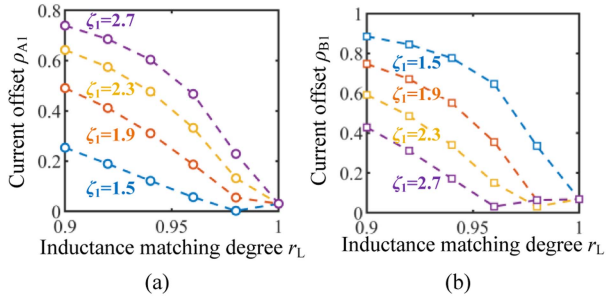

Fig. 6. Relationship between load current offset and inductance matching degree r_L. (a) ρ_{A1}. (b) ρ_{B1}.

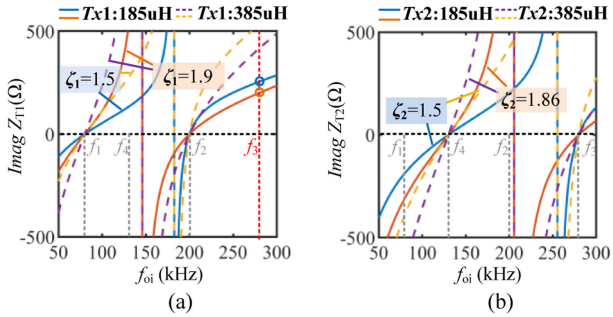

Fig. 7. Relationship between the L_{Tk}, ζ and the imaginary part of Z_{Tk} in the frequency domain ($r_L = 1$). (a) Tank #1. (b) Tank #2.

Then, L_{p1} and C_{pF1} can be calculated by (23) based on the preset ζ_1, and C_{p1} can be solved from

$$C_{p1} = \frac{1}{\omega_{p1}^2 L_{p1}} = \frac{\zeta_1}{\omega_2^2 L_{p1}}. \tag{24}$$

Similarly, the inductance and capacitance in X_{p2} and X_B can be obtained based on the preset ζ_2 and ζ_B.

From the above-mentioned calculation process of the MFRC network, it can be inferred that, after achieving the coil self-inductance and resonant frequency, the ratios ζ_1, ζ_2, and ζ_B determine the compensation parameters and impedance values of the MFRC networks X_{p1}, X_{p2}, and X_B, respectively. On one hand, ζ should be set greater than 1 to ensure that the solved compensation parameters are positive [24]. On the other hand, the sensitivity of the system to the values of compensation elements can be reduced by optimizing ζ.

Compensation capacitors are typically thin-film or ceramic capacitors, and precise matching can be achieved through series or parallel connections of capacitors. Errors and aging in manually wound compensation inductors may lead to compensation parameter offsets, thereby disrupting resonance states. Hence, the system performance should be evaluated when the inductance offset occurs. For MFRC networks, the inductance matching degree is defined as $r_L = L/L_{ideal}$, where L and L_{ideal} are the actual and ideal compensation inductance values, respectively. Using tank #1 as an example for analysis, the relationship between r_L and the transmitter impedance Z_{T1} is calculated by (8). As shown in Fig. 5, when mismatches of L_{p1} occur at resonant point $f_2 = 200$ kHz, it can be observed that the resonance state of tank #1 is disrupted, which may lead to a drop in load current. Comparing Fig. 5(a) and (b), ζ_1 changes from 1.5 to 1.9, which means the parallel LC unit resonant frequency f_{p1} moves away from point of 200 kHz. It can also be observed that the sensitivity of $Z_{T1}(\omega_{oi} = \omega_2)$ to r_L significantly decreases. This implies that the resonant points of the MFRC network should not be too close to the resonant point of the parallel LC unit, as it would increase the sensitivity of the system to compensation parameters.

When the operating frequency is f_j, the load current offset ρ_{mj} of the target phase m can be calculated by

$$\rho_{mj} = \frac{|I_{Lm} - I_{ref}|}{I_{ref}} \ (\omega_{oi} = \omega_j). \tag{25}$$

The relationship between r_L, ρ_{A1}, and ρ_{B1} is illustrated in Fig. 6. On one hand, with the decrease in r_L, the load current offset gradually increases. To maintain the target load current around I_{ref}, a certain level of compensation inductance accuracy must be ensured. On the other hand, with the same r_L ($r_L \neq 1$) and increase of ζ_1, the deviation rate of I_{LA} increases, leading to an increment in the sensitivity of channel A to r_L. Hence, reducing ζ_1 will decrease the sensitivity of channel A to r_L. However, reduced ζ_1 will increase the sensitivity of channel B to r_L. Thus, a compromise selection of ζ_1 is necessary to optimize the sensitivity of both channels simultaneously. This article selects the resonant point of the parallel LC unit near the average of the two target frequencies in the MFRC network. In tank #1, ζ_1 is set to 1.9, resulting in $f_{p1} = 145$ kHz, close to $(f_1+f_2)/2 = 140$ kHz.

Variations in ζ may result in a decrease in Z_{Tk} at nontarget resonance frequencies, leading to cross interference between tanks relayed by receiving coil B. Fig. 7 analyzes the impact of ζ and the inductance L_{TK} on the imaginary part of Z_{Tk}. As shown in Fig. 7(a), *Imag* $(Z_{Tk}) \approx 0\ \Omega$ at the target resonant frequencies of $f_1 = 80$ kHz and $f_2 = 200$ kHz. At the nontarget frequency of $f_3 = 280$ kHz, an increase in ζ_1 will decrease Z_{T1} at frequency of f_3. This may result in interference from tank #2 to tank #1. This article enhances the filtering performance of the tanks and reduces cross interference at nontarget frequencies by selecting transmitting coils with larger inductance of 385 μH. For the tank #2 as shown in Fig. 7(b), f_{p2} is selected near the average of f_3 and f_4, which is 205 kHz, close to one of the nontarget frequency, namely $f_2 = 200$ kHz. Due to the high impedance of the parallel LC unit at f_{p2}, tank#2 gets good filtering performance at f_2.

In conclusion, the main principles for calculating MFRC network parameters to ensure the resonant state and reduce the sensitivity are as follows.

1) Fully compensating the reactive power of the transmitting coil at the target resonant frequency.
2) Select the resonant point of the parallel LC unit near the center of the two target frequencies of the MFRC to reduce the system's sensitivity to compensating inductance values.
3) Supplement with sufficient self-inductance of the transmitting coil or appropriate resonant frequency design to enhance the interference resistance of tanks.

2) Design for ZVS: In order to reduce the switching losses of MOSFET-based inverters, it is necessary to operate the inverters in the ZVS mode. For the bridge inverter adopted in this article, the key issue to achieve ZVS lies in ensuring that the parasitic capacitance between the source and drain of the switching devices is fully discharged before the switching action. This requires that during the dead band, there is sufficient current flowing through the capacitor to ensure its rapid charging and discharging. Therefore, in the design stage of the inverter, the selection of switching devices and the optimization of PCB layout are of great importance to reduce the impact of parasitic capacitance on the circuit. In addition, it is relatively easy to indirectly achieve ZVS by adjusting the phase of the loop current [17], [18]. After the compensation components are precisely tuned at the working frequency, the parameter values of the compensation capacitor are dynamically adjusted to change the current phase, thereby achieving ZVS. Therefore, this article first optimizes the setting of the dead band so that the current flowing through the switching devices is close to zero when they are turned ON. Then, a method in [17] and [18] is adopted to ensure that the current lags behind the voltage when the switching devices are turned ON, thus creating conditions for achieving ZVS. Specifically, after a design focused on fully resonance, the MFRC parameters of the transmitter need to be fine-tuned to achieve $\varphi^{(i)}(\omega_{oi}) > 0$ at the operating angular frequency ω_{oi}. In this article, C_{pFk} is regulated to achieve ZVS of the inverter. The analysis of ZVS and balanced output is shown in Fig. 8, where the series capacitor in tank #*k* required for full resonance compensation can be denoted as C_{pFk0}.

As illustrated in Fig. 8(a) and (c), the inductive input impedance is roughly distributed in the yellow region of $C_{pFk}/C_{pFk0} > 1$, and satisfied values of C_{PFk} are in the set of $\Re_{zk}$. Moreover, the variations of C_{pFk} will also result in output current offset. Hence, C_{pFk} selection should meet the rated output and current balance requirements. As shown in Fig. 8(b) and (d), the green and blue regions represent the feasible C_{pFk} areas, where the current error is limited within $5\% \times I_{ref}$, and feasible values of C_{pFk} are in the set of $\Re_{pk}$. In addition, the sets of $\Re_{zk}$ and $\Re_{pk}$ vary with load. To achieve ZVS and balanced output simultaneously, the intersection of $\Re_{zk}$ and $\Re_{pk}$, namely $\Re_k = \Re_{zk} \cap \Re_{pk}$, should be taken. Then, the intersections of $\Re_k$ with varied loads, namely $\Re_{k'}$, are taken. Finally, minimize C_{pFk} to reduce the input impedance angle by selecting the minimum value within $\Re_{k'}$ to minimize switching-off losses.

3) Parasitic Parameters Analysis: The additional losses caused by the internal resistance of compensating components may affect the current balance state of the system. Since compensating capacitors are usually composed of multiple capacitors in parallel, their internal resistance can be neglected compared to compensating inductors. As a result, the relationship between the internal resistance of compensating inductors and the load current offset ρ_{mj} will be evaluated. When the internal resistance of compensating inductors is considered, the impedances of tank #1, tank #2, and receiver B, namely X_{p1}, X_{p2} and X_B, are defined as

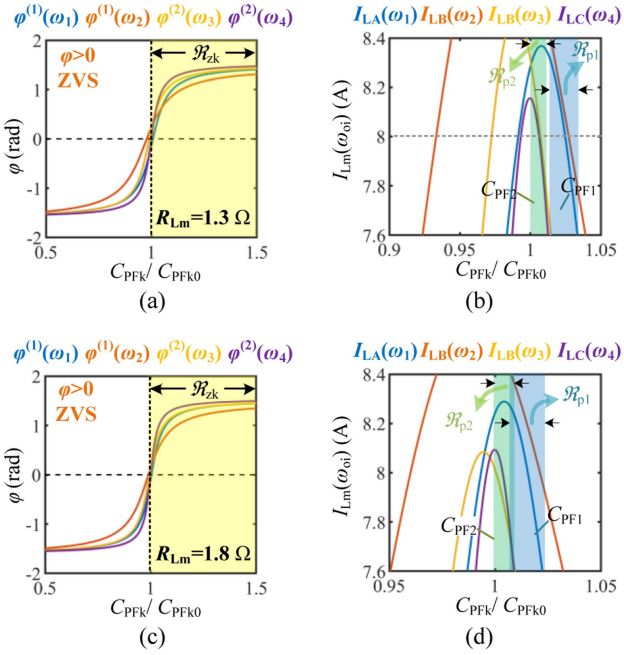

Fig. 8. Relationship between the C_{pFk}/C_{pFk0}, input impedance angle $\varphi^{(i)}(\omega_{oi})$ and load current $I_{Lm}(\omega_{oi})$ with varied loads. (a) $\varphi^{(i)}(\omega_{oi})$ with $R_{Lm} = 1.3\ \Omega$. (b) $I_{Lm}(\omega_{oi})$ with $R_{Lm} = 1.3\ \Omega$. (c) $\varphi^{(i)}(\omega_{oi})$ with $R_{Lm} = 1.8\ \Omega$. (d) $I_{Lm}(\omega_{oi})$ with $R_{Lm} = 1.8\ \Omega$.

$$X_{p1}(\omega) = -\frac{1}{\omega C_{pF1}} + (\omega L_{p1} + R_{p1}) // \left(-\frac{1}{\omega C_{p1}}\right) \quad (26)$$

$$X_{p2}(\omega) = -\frac{1}{\omega C_{pF2}} + (\omega L_{p2} + R_{p2}) // \left(-\frac{1}{\omega C_{p2}}\right) \quad (27)$$

$$X_B(\omega) = -\frac{1}{\omega C_B} + (\omega L_{B1} + R_{B1}) // \left(-\frac{1}{\omega C_{B1}}\right) \quad (28)$$

where R_{p1}, R_{p2}, and R_B are the resistances of L_{p1}, L_{p2}, and L_{B1}.

As shown in Fig. 9(a) and (b), an excessively high R_{p1} will result in the load current offset of phases A and B exceeding 5%, while variations in R_{p2} have little impact on ρ_{A1} and ρ_{B1}. This is because tank #1 only provides energy at frequencies f_1 and f_2 to phases A and B, respectively. Similarly, a large R_{p2} will lead to ρ_{B2} and ρ_{C2} exceeding 5%, as depicted in Fig. 9(c) and (d). Therefore, the internal resistance of the compensating inductors should be minimized as much as possible.

E. Summary of the System Circuit Design Procedure

As aforementioned, the system circuit design procedure is summarized in Fig. 10, and the parameters in Table I are utilized in experiments.

1) The transmitting and receiving coils are wound, and their self-inductance and internal resistance are measured. Subsequently, $\omega_{oi}M_{Tmk}$ can be calculated by (17) and verified for the current balance under varying loads using (16).

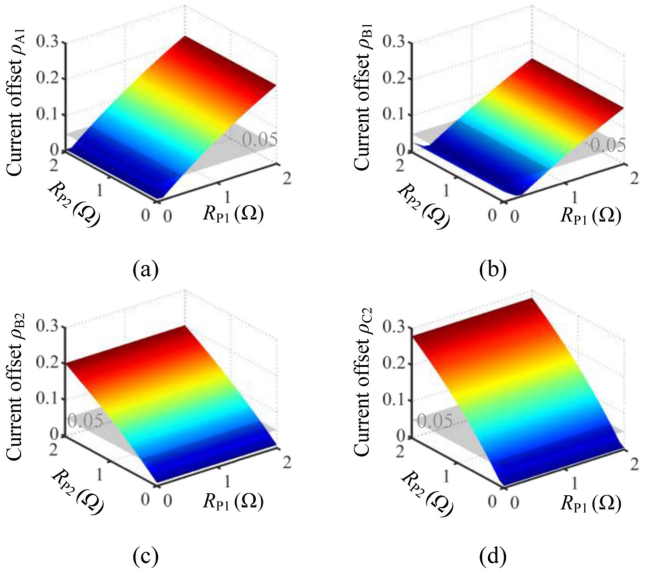

Fig. 9. Relationship between the resistance R_{p1}, R_{p2}, and load current offset ρ_{mj}. (a) ρ_{A1}. (b) ρ_{B1}. (c) ρ_{B2}. (d) ρ_{C2}.

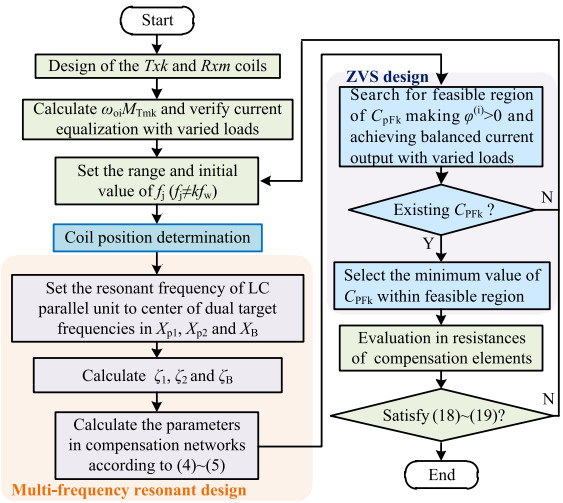

Fig. 10. Design flowcharts of the proposed four-channel based multifrequency resonant compensated WPT-SRM.

2) Initialize the resonant frequencies based on the constraint $f_j \neq kf_w$, along with calculating the expected mutual inductance values for load current equalization using $\omega_{oi}M_{Tmk}$ obtained in step one.
3) Iterate over Δ_{Tx} to achieve $M_{T12} = 0$. Meanwhile, M_{Tmk} can be adjusted by varying Δ_{Tmk} to match the expected mutual inductance values.
4) Select f_{p1}, f_{p2}, and f_{B1} near $(f_1 + f_2)/2$, $(f_3 + f_4)/2$, and $(f_2 + f_3)/2$, which are the center frequencies of the target frequencies in the MFRC networks X_{p1}, X_{p2}, and X_B, respectively. Subsequently, computing ζ_1, ζ_2, and ζ_B based on the definition of the ratio ζ in Section II-C. Then, the compensation parameters can be obtained through (4) and (5).

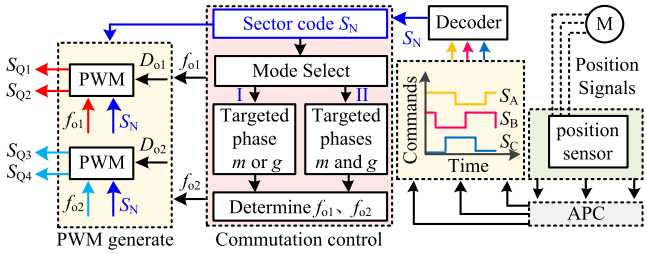

Fig. 11. Hybrid resonant excitation strategy.

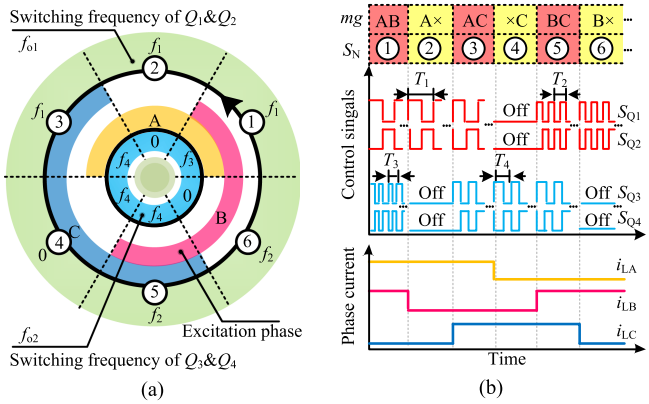

Fig. 12. Operating principles of the commutation control. (a) Commutation control and frequency selection logic. (b) Operating waves with $D_{o1} = D_{o2} = 50\%$.

5) Modify C_{PFk} to ensure that the input impedance angle $\varphi^{(i)}(\omega_{oi})$ is greater than 0, while maintaining load current balance.
6) Finally, evaluate the impact of component internal resistance on load current balance and verify the effectiveness of cross-interference suppression as described in (18) and (19).

F. Hybrid Resonant Excitation Strategy

Traditionally, the single-phase sequential excitation mode cannot full utilizing the inductance rising region to generate more positive torque, resulting in limited motor output. Generally, this excitation method is useless in real applications of SRM drives as its limited torque output and low efficiency. To overcome this problem, a hybrid resonant excitation strategy is developed for implementing the hybrid single-phase excitation and dual-phase excitation. Detailed operation principle is analyzed as follows.

The hybrid resonant excitation strategy is shown in Fig. 11, where the period $T_j = 1/f_j$, and D_{oi} is the pulsewidth of the inverter control signals. First, the rotor angle is resolved by position signals and then angular position control is utilized to generate the excitation commands S_A, S_B, and S_C. Then, the sector number of the commutation control sequence, namely S_N, can be achieved by decoding the commands. According to the commutation control sequence, the operating mode, targeted phase(s), and the operating frequencies are located in the sector S_N, as shown in Fig. 12(a). Finally, the driving signals S_{Q1}–S_{Q4} are generated. If DPEM is activated, both phase m and phase g are

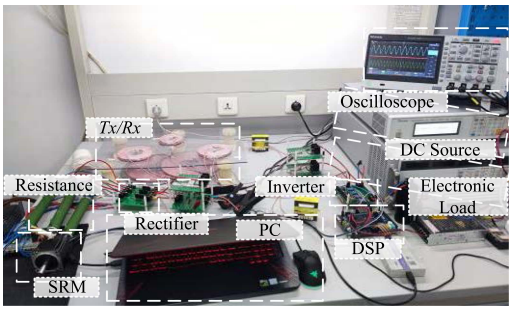

Fig. 13. Experimental prototype platform.

energized, while only one of the phases can be excited in SPEM. Taking the commutation sequence A-C-B as an example, the commutation control and frequency selection logics are shown in Fig. 12(a). In SPEM mode, when only A or only B phase is conducted, the Q_1/Q_2 of bridge leg I are controlled with PWM signals and Q_3/Q_4 of bridge leg II are turned OFF. The injected PWM frequency is f_1 and f_2 respectively. When phase C is the only conduction phase, the Q_3/Q_4 of phase leg II are active and Q_1/Q_2 are turned OFF. The injected PWM frequency is f_4. In DPEM, when phase A and C are excited, Q_1/Q_2 operate at frequency f_1 and Q_3/Q_4 operate at frequency f_4. When phase C and B are excited, Q_1/Q_2 operate at frequency f_2 and Q_3/Q_4 operate at frequency f_4. Similarly, when phase B and A are excited, Q_1/Q_2 operate at frequency f_1 and Q_3/Q_4 operate at frequency f_3. The operating waves are shown in Fig. 12(b). It should be noted that, if a bridge leg is controlled with PWM signals, it means the ideal driving signals S_Q of the two switches in the bridge leg are complementary.

IV. Experimental Results

An experimental test-bed is established to test the effectiveness of the proposed WPT-SRM system and its control method. As shown in Fig. 13, the test-bed mainly consists of modules such as a programmable dc source, FB inverter, DSP28335-based controller, resonant compensation circuits, transmission coil, diode bridge rectifier, and a 6/4 structure SRM. The system specifications are listed in Table I. In the experiments, the SPEM/DPEM driving operation, cross-interference suppression, current balance, and ZVS characteristics are tested for validation.

A. Cross Interference Suppression Tests

To evaluate the cross interference suppression capability of the proposed system, the ac current of the three receivers are measured under motor driving operation with the hybrid resonant excitation strategy. According to the commutation sequence as illustrated in Fig. 12, there is a six-step commutation combination in any electrical cycle, which is labeled as ①–⑥ in Fig. 14. Taking the commutation step ① as illustrated in Fig. 14(a), for example, *Tx*1 transmits power at a frequency of 80 kHz to excite phase A, while *Tx*2 transmits power at a frequency of 280 kHz to excite phase B. In this operation state, the current in the receiver of phase C is suppressed to zero. Similarly, in commutation step ②–④ as shown in Fig. 14(b)–(d), the current in the receiver of those nonconducted phases are also well suppressed. As shown in Fig. 14(e) and (f), only slight interference occurs in intervals

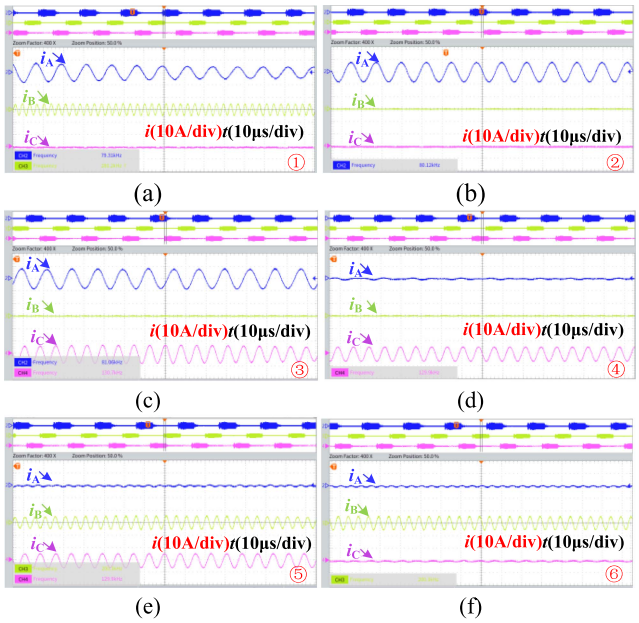

Fig. 14. The AC current on the receiver side under the hybrid resonant excitation strategy. (a) $f_{o1} = 80$ kHz, $f_{02} = 280$ kHz. (b) $f_{o1} = 80$ kHz, $f_{02} = 0$ Hz. (c) $f_{o1} = 80$ kHz, $f_{02} = 130$ kHz. (d) $f_{o1} = 0$ Hz, $f_{02} = 130$ kHz. (e) $f_{o1} = 200$ kHz, $f_{02} = 130$ kHz. (f) $f_{o1} = 200$ kHz, $f_{02} = 0$ Hz.

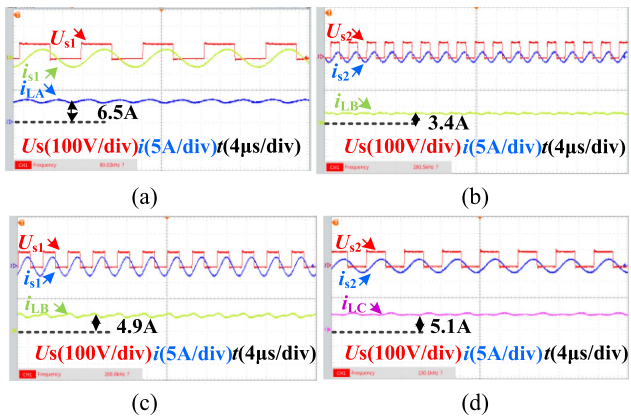

Fig. 15. Inverter voltage, current, and receiver-side DC current. (a) $f_{o1} = 80$ kHz, $f_{02} = 0$ Hz. (b) $f_{o1} = 0$ Hz, $f_{02} = 280$ Hz. (c) $f_{o1} = 200$ kHz, $f_{02} = 0$ Hz. (d) $f_{o1} = 0$ Hz, $f_{02} = 130$ kHz.

⑤ and ⑥. But as the interference evaluation factor γ_{Rxmk} is lower than 5%, the interference after the diode bridge rectifier can be neglected. Thus, the proposed system can effectively suppress interphase cross interference under both SPEM and DPEM motor drive operation.

B. Test and Analysis of the Current Balance

To analyze the current balance characteristic of the test system, the output current in different frequency channels are measured under resistive load conditions. As shown in Fig. 15, the tested output current is unbalance. Moreover, it is clear that the output current is lower with the increasing operation frequency. The reasons are discussed as follows.

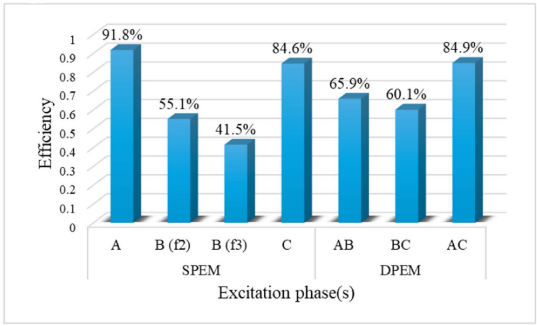

Fig. 16. Transmission efficiency under various excitation modes.

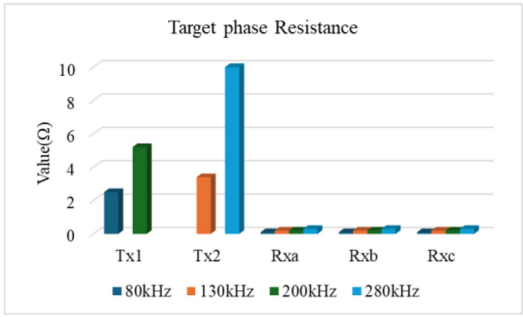

Fig. 17. Actual measured value of loop resistance.

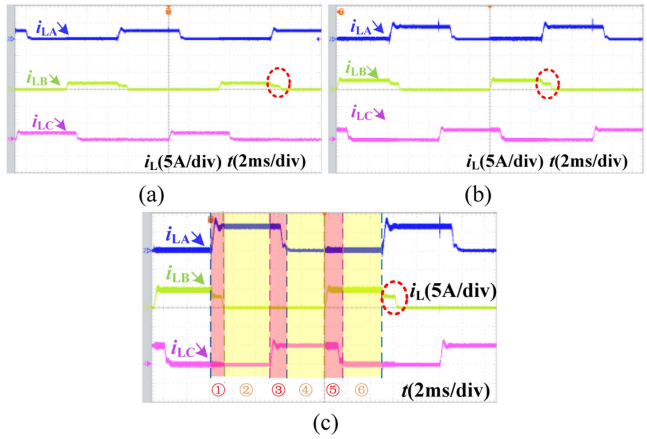

Fig. 18. Under resistive load conditions, the DC side current at the receiver based on hybrid excitation strategies. (a) $V_{\rm in} = 36$ V. (b) $V_{\rm in} = 56$ V. (c) $V_{\rm in} = 96$ V.

When the system operates at 200 kHz or 280 kHz, the circuit impedance value is even twice that of low frequency, resulting in a large amount of power consumption in the resonant circuit during high-frequency operation, leading to low system efficiency. With rated power operation, the transmission efficiency in different operating modes is analyzed in Fig. 16. In SPEM, as the frequency increases, the transmission efficiency shows a decreasing trend, which verifies the reason for the decrease in transmission efficiency caused by the increase in loop impedance due to the increase in frequency. It is worth noting that although the system operates with low efficiency at high frequencies, the overall low-efficiency working time accounts for a relatively short proportion of the entire cycle time. This also means that the overall efficiency of the system will not be at an extremely low value. The efficiency chart for each frequency excitation is shown in Fig. 16, and the overall efficiency reaches 76.1%.

According to (16), the load-side receiving current $I_{\rm Lm\_ind}$ is primarily related to the following factors.

1) $\omega_{\rm oi} \times M_{\rm Tmk}$ and $V_{\rm in}$: In this study, different operating frequencies are matched with different mutual inductances. The product of the mutual inductance $M_{\rm Tmk}$ between the coils and the operating frequency $\omega_{\rm oi}$ is set to be the same. Therefore, this factor will not cause output imbalance. In addition, the constant dc input voltage will not result in output imbalance.
2) $R_{\rm Tk} \times (R_m + R_{\rm Leqm})$: By measuring the resistance of the coupling coils and loops at different positions in the system, the reasons for the unbalanced output current are analyzed. As shown in Fig. 17, the actual wound coils have significant differences in internal resistance at different operating frequencies, and the resistance of the transmitting coils is much higher than that in the receivers. Moreover, the affections of the frequencies on transmitting coils are also much more obvious. In addition, the impedance characteristics of the resonant capacitor in the compensation circuit also change when the frequency changes, which cannot be ignored in practical operation. Therefore, the main reason for power imbalance is the significant difference in loop impedance at different frequencies.

The impedance of the transmission circuit during B-phase excitation is significantly higher than that during A-phase and C-phase excitation due to the two excitation frequencies of 200 and 280 kHz. Especially at a frequency of 280 kHz, the impedance reaches its maximum, resulting in a lower output. As can be seen in Fig. 18, under resistive load conditions, the output of phase B is significantly lower than that of phases A and C. In the transient instant from commutation step ⑥ to ①, the control frequency of phase B is changing from $f_2 = 200$ kHz and $f_3 = 280$ kHz, the output current experiences a step decrease due to the increase in impedance, which is consistent with the aforementioned discussion. The test results under motor driving operation are also given in Fig. 19. As can be seen in this figure, under the proposed hybrid resonant excitation strategies, the SRM can operate stably under both SPEM and DPEM modes with varied turn-ON and -OFF angles. However, the output current of phase B is significantly lower than that of phases A and C.

For further verifying the affection of the varied inner resistance of the transmitting coils under different frequencies on the output current balances, the test experiments with additional compensation resistors connected in the output terminals of phase A and C are implemented. These tests are used to mimic the difference in coil resistance between phase A and C conduction and phase B conduction. Since the entire excitation period of phase B at 280 kHz is relatively short, the additional compensation resistances are selected based on the measured transmitting coil resistances at 200 kHz. According to (16), the additional compensation resistance of phase A can be calculated from

$$(R_{\rm Tk}+R_{\rm Tk\_inc})(R_m+R_{\rm Leqm}) = R_{\rm Tk}(R_m+R_{\rm Leqm}+R_{\rm Lm\_ad}) \tag{29}$$

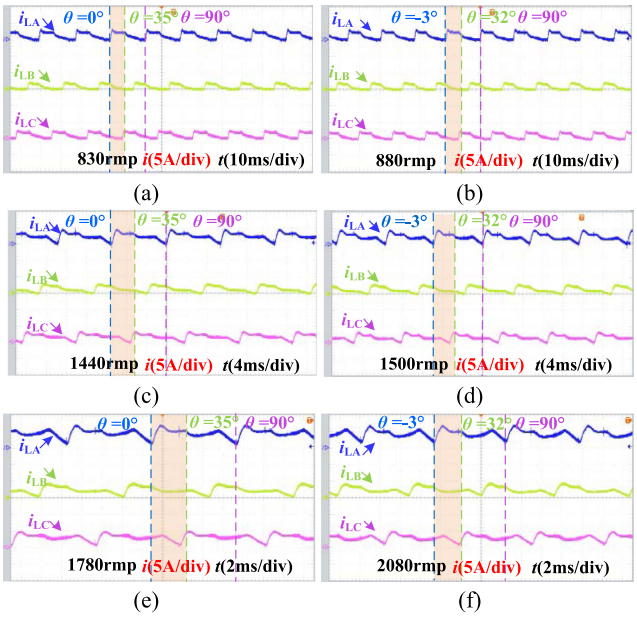

Fig. 19. Motor dive operation with hybrid excitation strategies. (a) $V_{\rm in} = 36$ V, $\theta_{\rm on} = 0°$, $\theta_{\rm off} = 35°$. (b) $V_{\rm in} = 36$ V, $\theta_{\rm on} = -3°$, $\theta_{\rm off} = 32°$. (c) $V_{\rm in} = 56$ V, $\theta_{\rm on} = 0°$, $\theta_{\rm off} = 35°$. (d) $V_{\rm in} = 56$ V, $\theta_{\rm on} = -3°$, $\theta_{\rm off} = 32°$. (e) $V_{\rm in} = 96$ V, $\theta_{\rm on} = 0°$, $\theta_{\rm off} = 35°$. (f) $V_{\rm in} = 96$ V, $\theta_{\rm on} = -3°$, $\theta_{\rm off} = 32°$.

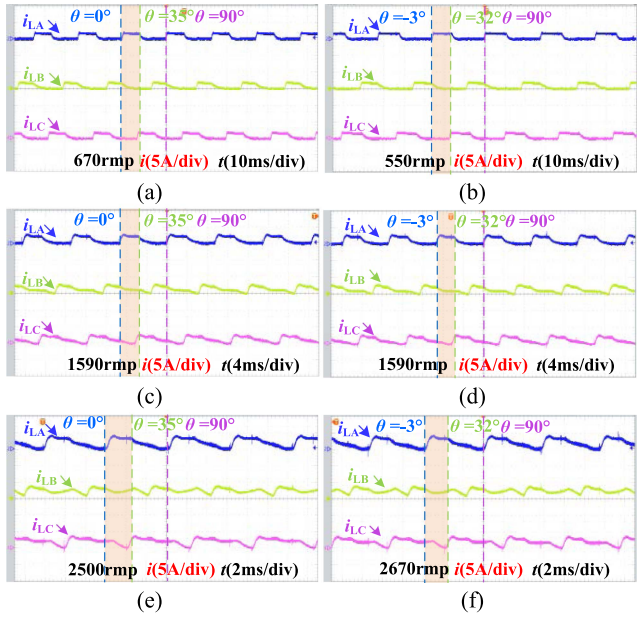

Fig. 20. Motor dive operation under hybrid excitation strategies with additional compensation resistors. (a) $V_{\rm in} = 36$ V, $\theta_{\rm on} = 0°$, $\theta_{\rm off} = 35°$. (b) $V_{\rm in} = 36$ V, $\theta_{\rm on} = -3°$, $\theta_{\rm off} = 32°$. (c) $V_{\rm in} = 56$V, $\theta_{\rm on} = 0°$, $\theta_{\rm off} = 35°$. (d) $V_{\rm in} = 56$ V, $\theta_{\rm on} = -3°$, $\theta_{\rm off} = 32°$. (e) $V_{\rm in} = 96$ V, $\theta_{\rm on} = 0°$, $\theta_{\rm off} = 35°$. (f) $V_{\rm in} = 96$ V, $\theta_{\rm on} = -3°$, $\theta_{\rm off} = 32°$.

where $R_{\rm Tk\_inc}$ is the increased resistance in transmit coil *Txk* at 200 kHz, $R_{\rm Lm\_ad}$ is the compensated resistance of phase *m*. When *k* is 1, *m* represents the phase A. When *k* is 2, *m* denotes the phase C. As $R_{\rm Tk\_inc}$ can be measured offline by injecting 200 kHz signal in the transmitting coils. The equivalent $R_{\rm Lm\_ad}$ in phase A and C can be calculated from (29).

By adding the compensation resistors in phase A and C, the motor drive operation under the hybrid excitation strategy with varied switching angles are also tested. Compared to the test results as shown in Fig. 19, with the same dc voltage input, the current of phase A and B are decreased due to the addition of compensation resistors. Thus, three-phase currents become more balanced in Fig. 20. Moreover, compared with traditional asymmetric half-bridge converter, no negative voltage demagnetization mode exists in the WPT SRM system, which may result in delayed demagnetization process and long tail current. Especially in high-speed operation, as can be seen in Fig. 19(e) and (f), the phase current cannot be demagnetized into zero in an electric period, which may result in high negative torque and thereby affecting the speed increase of the motor. The same cases exist in Fig. 20(e) and (f), especially in current of phase B. Compared to that in Fig. 18(e) and (f), the current of phase A and C can be demagnetized faster due to the adding of additional compensation resistors. As the input voltage increases, the addition of compensation resistors reduces the impact of negative torque, thereby can achieving higher speeds under the same voltage conditions.

In summary, the test results fully verified that the increased inner resistances of the transmitting coils in different high operation frequencies is the main reason to result in current unbalance in the proposed system. To overcome this problem, some possible solutions may exist, such as the following.

1) Replace the Litz wire with more strands to further reduce the coil internal resistance.
2) Optimize the choice of resonant frequency to reduce the problem of large differences in loop impedance during frequency switching.
3) Utilize the pulse density control method to further equalize the three-phase output.
4) Adopting pulse amplitude modulation to enhance the output during B-phase excitation.

C. ZVS Testing

Experiments were implemented to test the soft switching performance under motor drive operation with or without compensation resistors. As shown in Figs. 21 and 22, whether to add compensation resistors at the receiving end or not have no effect on the ZVS function of the transmitting end. The output current of the inverter lags behind the output voltage in both SPEM and DPEM modes, which indicates that the input impedance is inductive and the ZVS can be achieved.

D. Comparison With Some Typical Wireless SRM Systems

To evaluate the main features of the proposed WPT-SRM system, a comprehensive comparison of the proposed system with some typical traditional WPT-SRM systems has been conducted, as shown in Table II. Specifically, the system in [13] exhibits higher WPT efficiency, but the number of switches required is approximately twice that of the proposed system, and the active converter on the motor side is prone to frequent failures. In [17], a large number of switching devices are employed and it is unable to achieve output power balance and phase-overlap excitation, thereby failing to fully exploit the performance of the SRM. Although the system in [19] can fulfill the above-mentioned

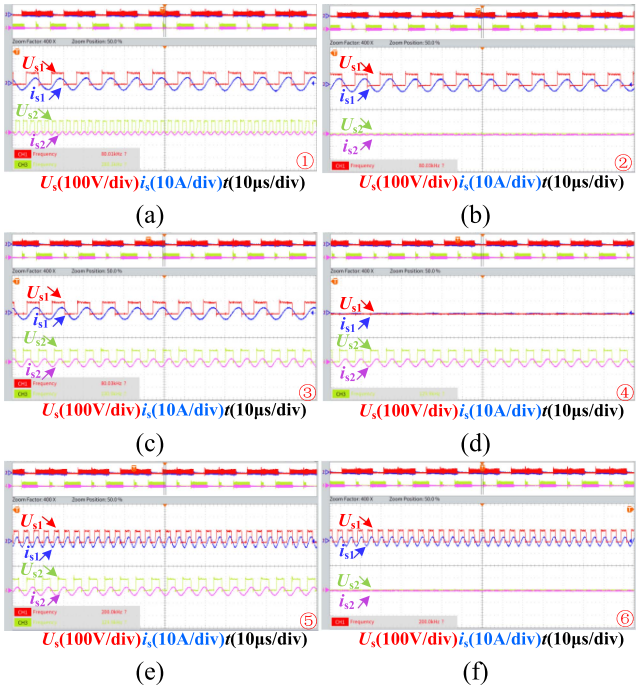

Fig. 21. Voltage and current in the dual transmitters under motoring operation without compensation resistors. (a) $f_{o1} = 80$ kHz, $f_{02} = 280$ kHz. (b) $f_{o1} = 80$ kHz, $f_{02} = 0$ Hz. (c) $f_{o1} = 80$ kHz, $f_{02} = 130$ kHz. (d) $f_{o1} = 0$ Hz, $f_{02} = 130$ kHz. (e) $f_{o1} = 200$ kHz, $f_{02} = 130$ kHz. (f) $f_{o1} = 200$ kHz, $f_{02} = 0$ Hz.

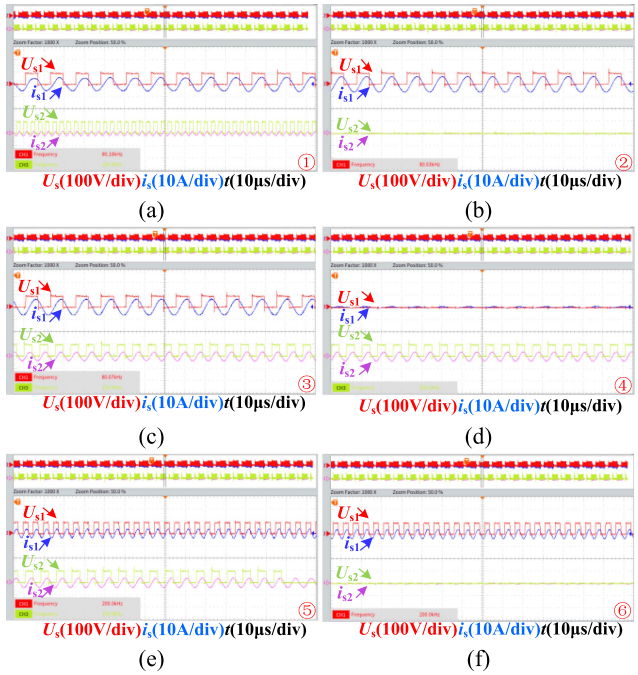

Fig. 22. Voltage and current in the dual transmitters under motoring operation with compensation resistor. (a) $f_{o1} = 80$ kHz, $f_{02} = 280$ kHz. (b) $f_{o1} = 80$ kHz, $f_{02} = 0$ Hz. (c) $f_{o1} = 80$ kHz, $f_{02} = 130$ kHz. (d) $f_{o1} = 0$ Hz, $f_{02} = 130$ kHz. (e) $f_{o1} = 200$ kHz, $f_{02} = 130$ kHz. (f) $f_{o1} = 200$ kHz, $f_{02} = 0$ Hz.

functions, it introduces a relatively large number of compensation devices, making the structure complex. Furthermore, during dual-frequency excitation, it is unable to achieve ZVS at both frequencies. The proposed topology in this paper can effectively address the problems existing in the aforementioned systems. Although output power balance has not yet been achieved due to the relatively high loop impedance when the multifrequency resonant loop operates at higher frequencies, the relevant reasons have been identified, and subsequent solutions have been formulated.

TABLE II
COMPARISON OF THE WPT-SRM SYSTEMS

Ref.	[13]	[17]	[19]	Proposed
Compensation	LCC-S	Switched capacitor-S	LCC-Trap filters& S	MFRC
Phase overlapped excitation	NO	NO	YES	YES
ZVS in dual-phase excitation	NO	NO	NO	YES
Power balances	YES	NO	YES	YES (*)
Number of switches	7	8	4	4
Number of frequencies	1	3	3	4
WPT efficiency	96%	72.8%	82.3	76.1%

* : Due to high-frequency working conditions, the high impedance of the circuit has temporarily not been achieved

V. CONCLUSION

In this article, a WPT-SRM system with ZVS characteristics and multifrequency resonance compensation is proposed. Detailed analysis of the system topology, design process, and experimental results are presented. The key features are as follows.

1) A WPT topology with dual decoupled resonant tanks on the transmitting side and hybrid compensation on the receiving side is developed for multifrequency resonant WPT and SPEM/DPEM hybrid SRM driving control. The optimized circuit modeling and design processes for this WPT-SRM are given.
2) The transmitter and receiver coil positions are optimally designed to suppress cross-interference at nontarget frequencies. Experimental results show that the proposed system can effectively suppress inter-phase cross interference under both SPEM and DPEM motor drive operation.
3) The multifrequency resonance compensation networks are optimized to achieve system current balance and single/dual loop ZVS of inverter with minimum input impedance angle. The test results show that the ZVS can be achieved under both SPEM and DPEM modes. However, the current balance is not well achieved due to the increased inner resistance of the transmitting coils in different high operation frequencies. Detailed experiments and comparisons are performed to verify this reason and affection factors. Moreover, some possible solutions for future studies are also given.
4) A hybrid resonance excitation strategy is also proposed to ensure stable driving operation of SRM in SPEM and DPEM hybrid modes. Experimental results fully verified the validity of the frequency-switching logics and the control scheme.

REFERENCES

[1] H. Feng, R. Tavakoli, O. C. Onar, and Z. Pantic, "Advances in high-power wireless charging systems: Overview and design considerations," *IEEE Trans. Transp. Electrific.*, vol. 6, no. 3, pp. 886–919, Sep. 2020.

[2] J. Choi, D. Tsukiyama, Y. Tsuruda, and J. M. R. Davila, "High-frequency, high-power resonant inverter with eGaN FET for wireless power transfer," *IEEE Trans. Power Electron.*, vol. 33, no. 3, pp. 1890–1896, Mar. 2018.

[3] Z. Dai and J. Wang, "A dual-frequency WPT based on multilayer self-decoupled compact coil and dual CLCL hybrid compensation topology," *IEEE Trans. Power Electron.*, vol. 37, no. 11, pp. 13955–13965, Nov. 2022.

[4] F. J. López-Alcolea, J. V. D. Real, P. Roncero-Sánchez, and A. P. Torres, "Modeling of a magnetic coupler based on single- and double-layered rectangular planar coils with in-plane misalignment for wireless power transfer," *IEEE Trans. Power Electron.*, vol. 35, no. 5, pp. 5102–5121, May 2020.

[5] Z. Hua, K. T. Chau, W. Han, W. Liu, and T. W. Ching, "Output-controllable efficiency-optimized wireless power transfer using hybrid modulation," *IEEE Trans. Ind. Electron.*, vol. 69, no. 5, pp. 4627–4636, May 2022.

[6] C. Xia, W. Wang, S. Ren, X. Wu, and Y. Sun, "Robust control for inductively coupled power transfer systems with coil misalignment," *IEEE Trans. Power Electron.*, vol. 33, no. 9, pp. 8110–8122, Sep. 2018.

[7] W. Liu, K. T. Chau, C. H. T. Lee, X. Tian, and C. Jiang, "Hybrid frequency pacing for high-order transformed wireless power transfer," *IEEE Trans. Power Electron.*, vol. 36, no. 1, pp. 1157–1170, Jan. 2021.

[8] H. Sekiya, K. Tokano, W. Zhu, Y. Komiyama, and K. Nguyen, "Design procedure of load-independent class-E WPT systems and its application in robot arm," *IEEE Trans. Ind. Electron.*, vol. 70, no. 10, pp. 10014–10023, Oct. 2023.

[9] W. Liu, K. T. Chau, C. H. T. Lee, L. Cao, and C. Jiang, "Frequency-modulated wireless direct-drive motor control," *IEEE Trans. Magn.*, vol. 57, no. 2, Feb. 2021, Art. no. 8201907.

[10] J. Cai, B. Li, W. Hua, A. D. Cheok, Y. Yan, and X. Zhang, "Magnetic coupled wireless motor driving systems – an overview," *IEEE Trans. Power Electron.*, vol. 39, no. 6, pp. 7375–7391, Jun. 2024.

[11] M. Sato, G. Yamamoto, D. Gunji, T. Imura, and H. Fujimoto, "Development of wireless in-wheel motor using magnetic resonance coupling," *IEEE Trans. Power Electron.*, vol. 31, no. 7, pp. 5270–5278, Jul. 2016.

[12] Y. Chen, C. Gan, H. Shi, K. Ni, Z. Yang, and R. Qu, "Auxiliary circuit free maximum power efficiency tracking scheme for wireless motor system with source-load coupling," *IEEE Trans. Ind. Electron.*, vol. 70, no. 4, pp. 3414–3425, Apr. 2023.

[13] W. Ding, K. Li, J. Yuan, J. Li, and C. Du, "Wireless power transmission-based In-wheel switched reluctance motor drive system with an x-type converter," *IEEE Trans. Energy Convers.*, vol. 38, no. 1, pp. 450–462, Mar. 2023.

[14] L. Fang et al., "Design of wireless individual-drive system for variable-reluctance stepping motor," *IEEE Trans. Circuits Syst. II-Exp. Briefs*, vol. 69, no. 4, pp. 2141–2145, Apr. 2022.

[15] W. Han, K. T. Chau, Z. Hua, and H. Pang, "An integrated wireless motor system using laminated magnetic coupler and commutative-resonant control," *IEEE Trans. Ind. Electron.*, vol. 69, no. 5, pp. 4342–4352, May 2022.

[16] C. Jiang, K. T. Chau, W. Liu, C. Liu, W. Han, and W. H. Lam, "An LCC-compensated multiple-frequency wireless motor system," *IEEE Trans Ind. Informat.*, vol. 15, no. 11, pp. 6023–6034, Nov. 2019.

[17] C. Jiang, K. T. Chau, C. Liu, and W. Han, "Design and analysis of wireless switched reluctance motor drives," *IEEE Trans. Ind. Electron.*, vol. 66, no. 1, pp. 245–254, Jan. 2019.

[18] K. Li, W. Ding, J. N. Yuan, and C. Du, "A decoupled multichannel based wireless SRM system with tunable compensation network and multifrequency pulse density control," *IEEE Trans. Ind. Electron.*, vol. 71, no. 2, pp. 1468–1480, Feb. 2024.

[19] J. Cai, B. Li, A. D. Cheok, Y. Yan, and X. Zhang, "Optimal design and control of a decoupled multifrequency multiphase wireless switched reluctance motor drive system," *IEEE Trans. Power Electron.*, vol. 39, no. 8, pp. 10152–10165, Aug. 2024.

[20] H. Wang, K. T. Chau, C. H. T. Lee, and C. Jiang, "Wireless shaded-pole induction motor with half-bridge inverter and dual-frequency resonant network," *IEEE Trans. Power Electron.*, vol. 36, no. 12, pp. 13536–13545, Dec. 2021.

[21] W. Liu, K. T. Chau, C. H. T. Lee, L. Cao, and W. Han, "Wireless power and drive transfer for piping network," *IEEE Trans. Ind. Electron.*, vol. 69, no. 3, pp. 2345–2356, Mar. 2022.

[22] H. Liu, H. Zhou, Q. Deng, W. Hu, X. Gao, and L. Fang, "A wireless dc motor drive using LCCC-CCL compensated network with bidirectional motion capability," *IEEE Trans. Circuits Syst. I- Reg. Papers*, vol. 69, no. 11, pp. 4714–4725, Nov. 2022.

[23] Z. Zhang, X. Li, H. Pang, H. Komurcugil, Z. Liang, and R. Kennel, "Multiple-frequency resonating compensation for multichannel transmission of wireless power transfer," *IEEE Trans. Power Electron.*, vol. 36, no. 5, pp. 5169–5180, May 2021.

[24] C. Qi, S. Huang, X. Chen, and P. Wang, "Multifrequency modulation to achieve an individual and continuous power distribution for simultaneous MR-WPT system with an inverter," *IEEE Trans. Power Electron.*, vol. 36, no. 11, pp. 12440–12455, Nov. 2021.

[25] Y. Liu, C. Liu, X. Gao, and S. Liu, "Design and control of a decoupled multichannel wireless power transfer system based on multilevel inverters," *IEEE Trans. Power Electron.*, vol. 37, no. 8, pp. 10045–10060, Aug. 2022.

[26] K. Li and W. Ding, "An improved one-to-three WPT system with tunable compensation network and enhanced pulse density voltage control," *IEEE J. Emerg. Sel. Top. Power Electron.*, vol. 11, no. 3, pp. 3586–3596, Jun. 2023.

Jun Cai (Senior Member, IEEE) received the Ph.D. degree in electrical engineering from the Nanjing University of Aeronautics and Astronautics, Nanjing, China, in 2012.

He is a Professor with the Nanjing University of Information Science and Technology, Nanjing, China. He is the Fellow of the Royal Society for the Encouragement of Arts, Manufactures and Commerce (RSA Fellow). His research interests include motor drives and control.

Bin Li received the B.Eng. degree in electrical engineering from the School of Automation, Nanjing University of Information Science and Technology, Nanjing, China, in 2021. He is currently working toward the M.Sc. degree in electronic information with Nanjing University of Information Science and Technology.

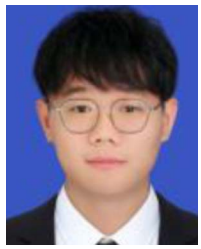

Yangyang Chen received the B.Eng. degree in electrical engineering from the School of Automation, Huangshan University, Huangshan, China, in 2021. He is currently working toward the M.Sc. degree in electronic information with Nanjing University of Information Science and Technology, Nanjing, China.

Shoujun Song (Senior Member, IEEE) received the Dr.-Ing. degree in electrical engineering from the Technical University of Berlin, Berlin, Germany, in 2009.

He is currently a Professor with the School of Automation, Northwestern Polytechnical University, Xi'an, China. His research interests include electric machines and drives in more electric aircraft.

Xin Zhang (Senior Member, IEEE) received the Ph.D. degree in automatic control and systems engineering from the University of Sheffield, Sheffield, U.K., in 2016, and the Ph.D. degree in electronic and electrical engineering from the Nanjing University of Aeronautics and Astronautics, Nanjing, China, in 2014.

He is currently a Professor with Zhejiang University, Hangzhou, China. His research interests include power electronics and advanced control theory.